Dalton Transactions

PAPER

View Article Online
View Journal | View Issue

Cite this: *Dalton Trans.*, 2016, **45**, 552

In situ photo-assisted deposition and photocatalysis of $ZnIn_2S_4$/transition metal chalcogenides for enhanced degradation and hydrogen evolution under visible light†

Wei Yang Lim,[a] Minghui Hong[a] and Ghim Wei Ho*[a,b]

Received 27th September 2015,
Accepted 9th November 2015

DOI: 10.1039/c5dt03775a

www.rsc.org/dalton

The effective immobilization of a transition chalcogenide co-catalyst *via* an *in situ* aqueous photo-assisted deposition technique has shown great accessibility to complex $ZnIn_2S_4$ host hierarchical nanostructured materials with homogeneous distribution. The complementary photo-assisted deposition readily deposits finely-dispersed co-catalyst particles and simultaneously generates photocatalytic hydrogen. Another added advantage is that the photo-assisted deposition of the co-catalyst does not compromise the crystal structure or the integrity of the host photocatalyst, hence offering a better alternative to the doping technique. A systematic study of various transition metal chalcogenide co-catalysts and optimization of wt% MoS_2, CuS and Ag_2S loadings were demonstrated. Among them, the $ZnIn_2S_4/MoS_2$ composite exhibits exceptional photocatalytic hydrogen production and stability as well as superior MO degradation under visible light irradiation. The present methodology is expected to be extendable to various transition metal oxides/chalcogenides since ionic derivatives exhibit high affinity to a variety of materials under photoirradiation.

1. Introduction

Extensive efforts towards the development of various oxide photocatalysts have been devoted since the discovery of photocatalytic water splitting on TiO_2 by Fujishima and Honda in 1972.[1,2] However to improve the feasibility of their practical application, recent research is focused on the study of visible-light-responsive photocatalysts.[3–5] Among the various photocatalysts, sulphide semiconductor photocatalysts have attracted much research attention due to their exceptional solar spectrum responses and high photocatalytic activities especially in the visible light region. The sulphide semiconductor photocatalysts usually possess relatively high conduction band positions appropriate for H_2O reduction and a higher valence band position of S 3p orbitals compared to that of oxides with a deep valence band position of O 2p orbitals. Such band edge positions favorably result in a smaller band gap and higher visible light absorption capabilities compared to oxides.[6]

The construction of metal sulphide photocatalysts *via* a low temperature solution method has recently been demonstrated as one of the viable approaches for formulating photocatalysts with excellent photocatalytic performances under visible light irradiation due to their controllable band structures and optimized contact interface for enhanced heterojunction-induced charge transfer.[7,8] Ternary chalcogenide $ZnIn_2S_4$ has attracted much interest because of its simplicity in materials synthesis, chemical stability against photocorrosion[9,10] and low toxicity.[11,12] Structural and electronic modifications to the $ZnIn_2S_4$ photocatalyst have been carried out by controllably synthesizing high surface area morphologies, *i.e.* microspheres, nanowires and nanotubes[13,14] and doping it with various transition metals,[15,16] alkaline-earth metals[17] and rare earth elements[18] in an attempt to improve its photocatalytic performance to a certain degree. It has been reported that co-catalysts enhance photocatalytic activity through separation of photo-excited carriers, lowering of activation potential for hydrogen evolution and also by furnishing redox reaction sites for hydrogen evolution to avoid back reactions.[19] However, reliable *in situ* loading of relatively inexpensive co-catalyst materials remains largely unexplored as most co-catalyst loading methods involve secondary processing often with a

[a]*Department of Electrical and Computer Engineering, National University of Singapore, Singapore 117576, Singapore. E-mail: elehgw@nus.edu.sg; Fax: +65 67754710; Tel: +65 65168121*
[b]*Institute of Materials Research and Engineering, A*STAR (Agency for Science, Technology and Research), 3 Research Link, 117602, Singapore*
†Electronic supplementary information (ESI) available. See DOI: 10.1039/c5dt03775a

temperature annealing step which imposes complexity and increases the cost of catalyst production.[20–23]

Herein, a facile loading of transition chalcogenide co-catalysts is demonstrated on $ZnIn_2S_4$ with hierarchical nanosheet structures *via* a low-temperature *in situ* photo-assisted deposition method. The *in situ* photo-assisted deposition presents five advantages: (i) a superior interfacial contact between the photocatalyst and the co-catalyst that facilitates effective charge carrier separation as compared to physical mixing and general chemical synthesis,[24,25] (ii) a concurrent process of co-catalyst deposition and photocatalytic H_2 evolution, (iii) homogeneous dispersion of co-catalyst particles across the whole photocatalyst surfaces,[26,27] (iv) direct formation of the co-catalyst in a fairly short duration with excellent reproducibility,[28] and (v) a facile solution-based technique at room temperature and mild conditions that warrants low cost manufacturability. This simple and convenient method, the photo-assisted deposition of a co-catalyst onto a photocatalyst, does not compromise the crystal structure or the integrity of the host photocatalyst, hence offering a better alternative to the doping technique. To the best of our knowledge, this is the first systematic study on the immobilization of finely dispersed transition metal chalcogenide co-catalysts and optimization of wt% loading *via* an *in situ* aqueous photo-assisted technique onto hierarchical $ZnIn_2S_4$ microspheres. The composite exhibits excellent photocatalytic hydrogen production and stability as well as superior MO degradation under visible light irradiation.

2. Experimental

2.1 Reagents and chemicals

Zinc chloride ($ZnCl_2$), indium chloride ($InCl_3$), thioacetamide (TAA), (1-hexadecyl)trimethyl ammonium bromide (CTAB), L(+) lactic acid 90%, copper acetate monohydrate ($Cu(Ac)_2{\cdot}H_2O$), silver nitrate ($AgNO_3$), and ammonium tetrathiomolybdate ($(NH_4)_2MoS_4$) were of analytical grade and used as received without further purification.

2.2 Synthesis of $ZnIn_2S_4$ nano-petal-assembled microspheres

Hexagonal $ZnIn_2S_4$ microspheres were prepared through the following procedures: 0.59 mmol $ZnCl_2$, 1 mmol $InCl_2$, an excess of TAA (3 mmol) and 150 mg CTAB were dissolved in 35 mL of deionized water and transferred into a Teflon-lined stainless steel autoclave of 50 ml capacity. The autoclave was then put in a heating oven, and maintained at 160 °C for 6 h. A yellow precipitate was obtained, which was washed with water and ethanol three times and dried for 90 min at 80 °C.

2.3 Loading of the co-catalyst *via* photo-assisted deposition

An *in situ* photo-assisted co-catalyst loading process was performed in concurrent with photocatalytic hydrogen evolution which is shown in Section 2.5. Different precursors, $Cu(Ac)_2{\cdot}H_2O$, $AgNO_3$ and $(NH_4)_2MoS_4$, were used to load Cu, Ag and MoS_2 onto $ZnIn_2S_4$ respectively. Various co-catalyst loading amounts were prepared by controlling the dissolution amount of precursors in the photocatalytic solution while keeping other conditions the same. All the stated co-catalyst loadings refer to the amount of added precursors while the approximate resulting co-catalyst loadings are determined by energy dispersive X-ray spectroscopy (EDX) (Fig. S1†).

2.4 Characterization

A field-emission scanning electron microscope (FESEM, JEOL FEG JSM 7001F) equipped with an EDX, operating at 15 kV was used to characterize the morphology of the synthesized products while both the X-ray diffractometer (XRD, Philips X-ray diffractometer equipped with graphite-monochromated Cu-Kα radiation at λ = 1.541 Å) and the transmission electron microscope (TEM, Phillips FED CM300) were used to analyze the crystallographic structure of the synthesized products. X-ray photoelectron spectroscopy (XPS) spectra were recorded on a VG Thermo Escalab 220I-XL system. All binding energies were referred to the C 1s peak of 284.8 eV. Absorption spectra of the samples were acquired using a Shimadzu UV-3600 UV-VIS-NIR spectrophotometer. Hydrogen uptake was measured using the pressure composition isotherm measurement on a Shimadzu GC-2014AT gas chromatographer.

2.5 Photocatalytic water splitting

All photocatalytic reactions were conducted in a quartz cylindrical glass tube of 25 mL volume. 10 mg as-prepared $ZnIn_2S_4$ powder, a proper amount of the co-catalyst precursor, 9 mL of deionized water and 1 mL of lactic acid as the sacrificial reagent were dispersed in the quartz tube by sonication for 2 min. Prior to photocatalytic water splitting and *in situ* photo-assisted deposition, these quartz tubes were sealed and purged with argon gas for 10 min. The measurements of H_2 evolution were carried out by magnetically stirring under visible light illumination from a 300 W xenon arc lamp equipped with a cut-off filter (λ > 400 nm). The readings were taken every 30 min over 2 h. Later, all as-prepared $ZnIn_2S_4$ and photo-deposited $ZnIn_2S_4$ were washed in water and ethanol, and then subjected to purging and photocatalytic water splitting under the same conditions but in the absence of a cut-off filter and a co-catalyst precursor. The readings were also taken every 30 min over 2 h. The photocatalytic H_2 evolution cycle test was carried out on photo-deposited $ZnIn_2S_4$ in 10 wt% lactic acid aqueous solution under visible light irradiation from a 300 W xenon arc lamp equipped with a cut-off filter (λ > 400 nm), with each cycle of 2 h duration. The readings were taken every 30 min over 2 h as well.

2.6 Photocatalytic degradation

The photodegradation activity was evaluated by the decomposition of methyl orange (MO) in an aqueous solution under visible light illumination. 10 mg of $ZnIn_2S_4$ or photo-deposited $ZnIn_2S_4$, 0.5 ml H_2O_2 and 10 ml of MO solution with 20 mg L^{-1} concentration were mixed in a quartz cylindrical glass tube to form a mixture of the photocatalyst and the dye. The quartz tubes were then magnetically stirred under illumination from a 300 W xenon arc lamp equipped with a cut-off

filter (λ > 400 nm). The photocatalyst-dye solution was centrifuged at 4000 rpm for 1 min before every absorbance scan in 3 ml of the dye solution. The maximal absorbance values (at 462.5 nm) obtained from a UV-VIS-NIR spectrophotometer were noted as an indicator of MO concentration, which corresponds to the amount of MO degraded within a given time interval.

3. Results and discussion

Fig. 1a and b show the FESEM images of the $ZnIn_2S_4$ microstructure; it can be clearly observed that the $ZnIn_2S_4$ crystallites were well self-assembled into nano-petals with a microsphere morphology (average diameter of 1 μm). Further investigations on the morphology and the crystallographic structure were carried out by TEM. From the TEM images depicted in Fig. 1c–e, it can be seen that the $ZnIn_2S_4$ floriated microsphere is made up of two-dimensional nano-petals. The high resolution (HR) TEM images of petals on the microsphere are shown in Fig. 1f, with an interplanar spacing of 0.32 nm, assigned to the (102) plane of hexagonal $ZnIn_2S_4$.[29] XRD and EDX of $ZnIn_2S_4$ are presented in Fig. 1g and h, respectively. All XRD diffraction peaks can be fully indexed to the hexagonal $ZnIn_2S_4$ phase (JCPDS-65-2023) with no peaks attributed to ZnS, In_2S_3 or an oxide, indicating high purity phase formation.[27] Furthermore, the Zn : In molar ratio of $ZnIn_2S_4$ microspheres measured by EDX corresponds to the molar ratio of the added Zn and In metal salts (Fig. S1†). This implies that homogeneous dissolution and precipitation of Zn^{2+} and In^{3+} metal ions occur which resulted in the formation of $ZnIn_2S_4$ microspheres.

Photo-assisted deposition of the co-catalyst onto the $ZnIn_2S_4$ photocatalyst was conducted concurrently with photocatalytic H_2 production under visible light irradiation. Prior to the light irradiation, individual $Cu(Ac)_2$, $AgNO_3$ and

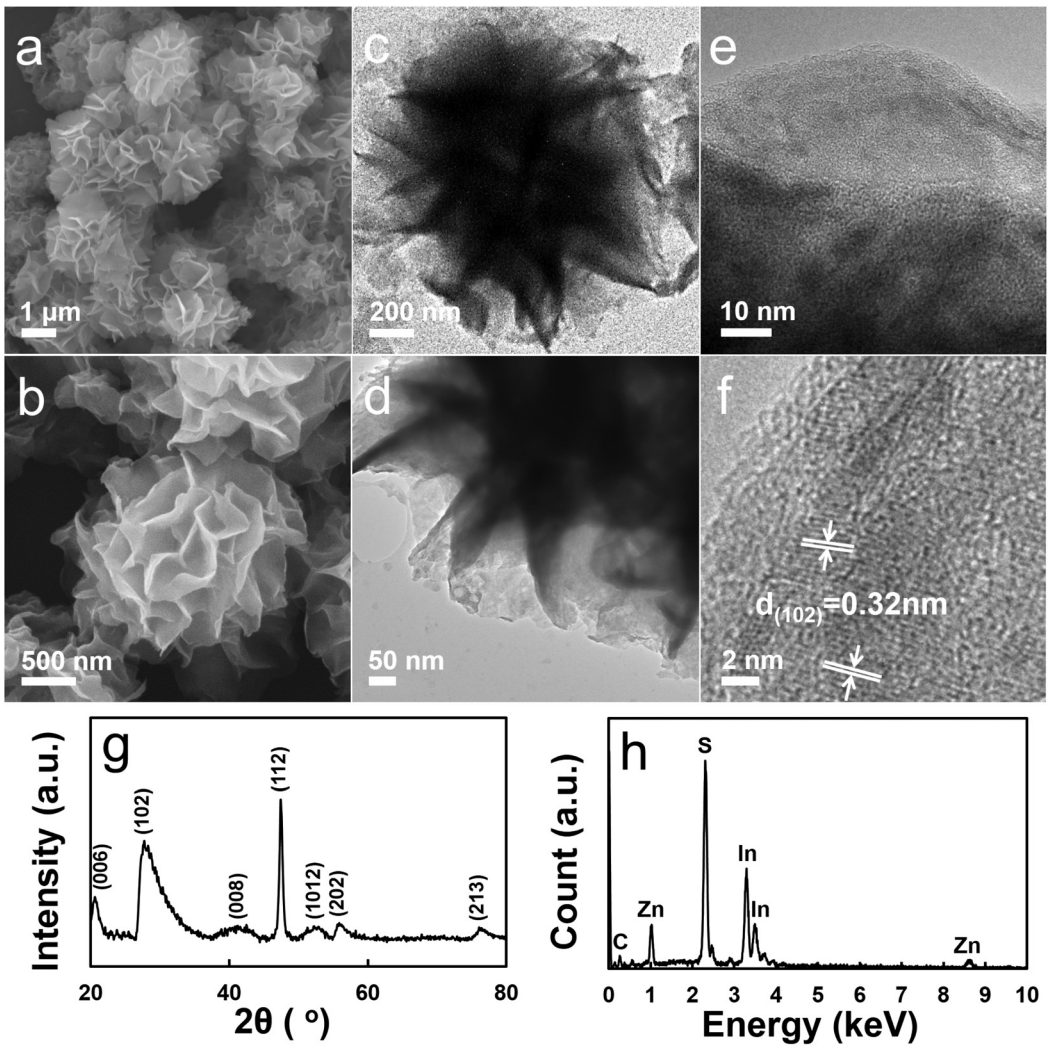

Fig. 1 (a and b) SEM and (c–e) TEM images of $ZnIn_2S_4$ microspheres. (f) HRTEM image of nano-petals, showing clear crystal fringes with 0.32 nm spacing. (g) XRD pattern and (h) EDX of $ZnIn_2S_4$ microspheres.

$(NH_4)_2MoS_4$ precursors were mixed in a photocatalytic assay solution to deposit CuS, Ag_2S and MoS_2 co-catalysts respectively. Fig. 2 shows the XPS spectra of pristine $ZnIn_2S_4$ microspheres and various transition metal chalcogenides, Ag_2S, CuS and MoS_2 loaded $ZnIn_2S_4$ microspheres. The peak positions of Zn, In, and S of pristine $ZnIn_2S_4$ microspheres agree with the literature,[30] indicating successful formation of $ZnIn_2S_4$ in the desired elemental composition. Moreover, the characteristic peaks of Cu, Ag and Mo are consistent with CuS, Ag_2S and MoS_2 references which were detected in the respective co-catalyst loaded $ZnIn_2S_4$, microspheres (Fig. 2d–f). This demonstrates the effectiveness of the photo-assisted deposition of various transition metal co-catalysts onto host $ZnIn_2S_4$ microspheres. The Zn 2p and In 3d peaks of co-catalyst loaded $ZnIn_2S_4$ microspheres were shifted to a lower binding energies[31,32] while the S^{2-} peak was shifted to a higher binding energy. Such a shift in the binding energy suggests a strong electronic coupling between $ZnIn_2S_4$ and the co-catalyst. The electron transfer from $ZnIn_2S_4$ to co-catalysts can be facilitated[20] and it is expected to enhance photocatalytic activities upon CuS, Ag_2S and MoS_2 co-catalysts loading.

In addition, TEM analysis was conducted on MoS_2 loaded $ZnIn_2S_4$ microspheres to investigate the morphology of photo-deposited co-catalyst. From the low magnification TEM image (Fig. 3a), it is clear that the microsphere structure comprises of nano-petals which are well-retained after the photo-assisted co-catalyst deposition process. Moreover, finely dispersed nanoparticles could be found to be distributed throughout the whole microspheres (Fig. 3b). On close inspection, the lattice fringes from the HRTEM image of the nano-petals in Fig. 3c show an interplanar spacing of 0.32 nm, which is consistent with the earlier TEM result of pristine $ZnIn_2S_4$ microspheres as shown in Fig. 1f. This validates the non-destructive nature of the *in situ* photo-assisted co-catalyst deposition process. It is noted that the finely dispersed co-catalyst nanoparticles do not display any characteristic lattice fringes, suggesting the amorphous state of the MoS_2 nanoparticles. Although amorphous MoS_2 generally lacks well-defined Mo edge sites, the presence of numerous defect sites renders many unsaturated sulfur atoms, which serve as hydrogen adsorption sites and ultimately lead to hydrogen evolution.[20]

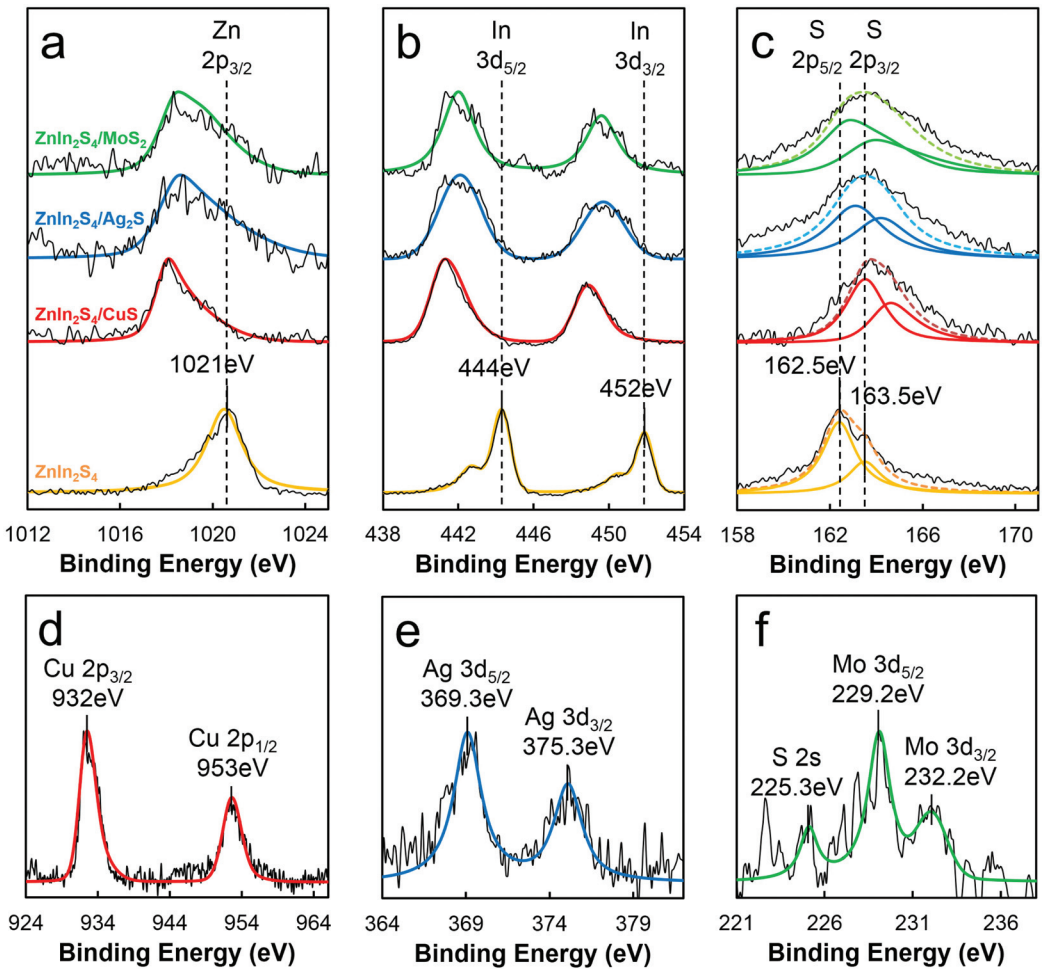

Fig. 2 XPS spectra of $ZnIn_2S_4$ (yellow), CuS-loaded $ZnIn_2S_4$ (red), Ag_2S-loaded $ZnIn_2S_4$ (blue) and MoS_2-loaded $ZnIn_2S_4$ (green): (a) Zn $2p_{3/2}$, (b) In 3d, (c) S $2p_{3/2}$, (d) Cu 2p, (e) Ag 3d, (f) Mo 3d core-level spectra.

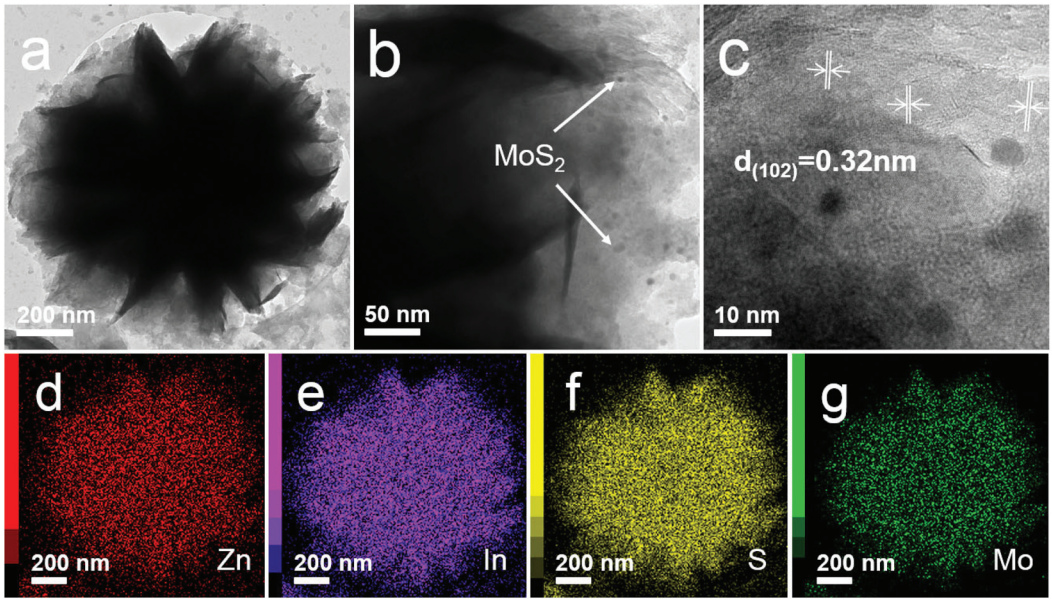

Fig. 3 (a and b) TEM and (c) HRTEM images of MoS_2 loaded $ZnIn_2S_4$. TEM mapping of uniformly distributed (d) Zn, (e) In, (f) S and (g) Mo elements of the microsphere.

TEM elemental mappings were carried out to study the composition and distribution of $ZnIn_2S_4/MoS_2$ microspheres. The images in Fig. 3a and d–g correspond to the acquired bright field images of Zn, In, S and Mo elements respectively. It can be seen that all the elements are uniformly distributed throughout the microsphere. While Zn, In and S signals are ascribed to the host $ZnIn_2S_4$ microsphere, an additional Mo signal of lower density appeared to be scattered across the microsphere. On the basis of the TEM and XPS analyses, the uniformly and finely dispersed nanoparticles can be attributed to MoS_2. Hence, this corroborates the homogeneous deposition of nanosized co-catalyst particles onto $ZnIn_2S_4$ microspheres by using the facile *in situ* photo-assisted deposition method.

The XRD patterns of $ZnIn_2S_4$ loaded with different transition metal chalcogenide co-catalysts *via* photo-assisted deposition are shown in Fig. 4a–d. Fig. 4a shows a pristine $ZnIn_2S_4$ microsphere diffraction pattern which correlates with the high purity hexagonal $ZnIn_2S_4$ phase. The MoS_2 loaded $ZnIn_2S_4$ microspheres show a similar diffraction pattern (Fig. 4d) as pristine $ZnIn_2S_4$ microspheres. This suggests that the photo-assisted deposition of MoS_2 produces finely dispersed amorphous nanoparticles. On the other hand, the Ag_2S and CuS loaded $ZnIn_2S_4$ microspheres show characteristic monoclinic phase Ag_2S (JCPDS-14-0072) and hexagonal phase CuS (JCPDS-06-0464) diffraction peaks.[33,34] The absence of Ag and Cu characteristic diffraction peaks may suggest that the oxidation process occurs and thereafter the photo-assisted deposition reduction process takes place. As Zn, In, Ag and Cu have rather similar atomic radii, Ag and Cu ions may be introduced into the host lattice as impurities. Consequently, these impurities disrupt the atomic crystal arrangement as observed from the diminished (006) $ZnIn_2S_4$ peak[35] (Fig. 4a). The incorporation of these ions into the host lattice forms interface coupling which leads to the formation of CuS and Ag_2S by the photo-generated holes from $ZnIn_2S_4$. This corroborates with the XRD result in Fig. 4b and c which presents the diminished $ZnIn_2S_4$ (006) facet attributed to the oxidation process that eventually leads to the formation of CuS and Ag_2S chalcogenides. Such an observation of crystal structure modification by photo-assisted deposition was also reported in the Au–CdS system.[36]

$ZnIn_2S_4$ was previously reported to be a direct band gap material[37] of 2.2 to 2.8 eV depending on the phase, particle size and morphology.[38,39] A UV-VIS-NIR spectrophotometer was employed to determine the band gap and compare the absorption spectra among the various $ZnIn_2S_4$ microspheres with different co-catalysts and variable wt% loading. All the absorption spectra were obtained in a wavelength range of 300 to 800 nm and are plotted in Fig. 4e–g. The band gap of $ZnIn_2S_4$ was determined using the following eqn (1):

$$(\alpha h\nu)^n \sim (h\nu - E_g) \quad (1)$$

where α and $h\nu$ are the absorption coefficient and the photon energy respectively, and the value of n corresponds to 2 for direct transition and $\frac{1}{2}$ for indirect transition.[40–42] The band gap of $ZnIn_2S_4$ was estimated to be 2.64 eV which agrees well with the reported value.[43,44] It can be observed from Fig. 4e–g that the light absorption of the photocatalyst was enhanced by all three co-catalysts particularly in the visible light range. The absorption was further enhanced with increasing co-catalyst wt% deposition. The appreciation of light absorption in the visible light range was confirmed visibly from the color alteration of $ZnIn_2S_4$ composite microspheres. The pristine $ZnIn_2S_4$

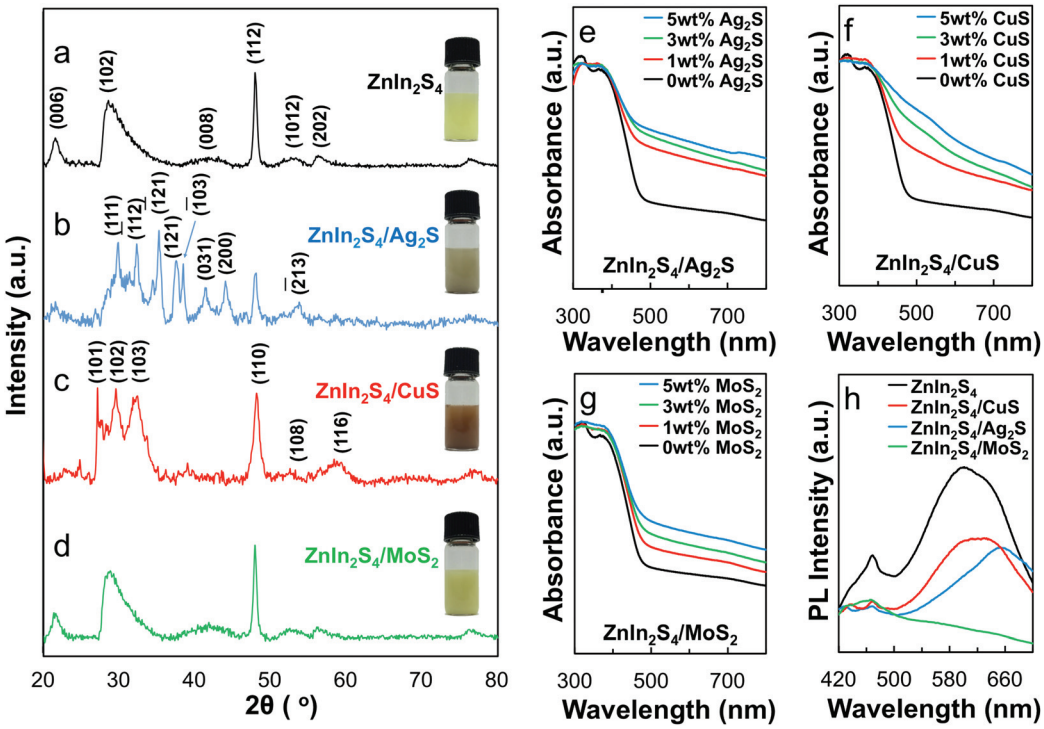

Fig. 4 XRD patterns of (a) $ZnIn_2S_4$ and $ZnIn_2S_4$ loaded with (b) Ag_2S, (c) CuS and (d) MoS_2 *via* photo-assisted deposition. Insets show the vials containing the respective samples. UV-vis absorption spectra of $ZnIn_2S_4$ loaded with different amounts of (e) Ag_2S, (f) CuS and (g) MoS_2. Photoluminescence emission spectra (h) of $ZnIn_2S_4$ and the photo-deposited $ZnIn_2S_4$ product. The additional parentheses number in curves (b) and (c) corresponded to the diffraction patterns of Ag_2S and CuS respectively.

microspheres present as a bright yellow powder whereas the colors of Ag_2S, CuS and MoS_2-loaded $ZnIn_2S_4$ were modified to greyish, brownish and dark yellowish, respectively (Fig. 4a–d insets). The extent of color change transitions is in agreement with the intensity of light absorption enhancement. In this case, the Ag_2S and CuS-loaded $ZnIn_2S_4$ exhibit a more drastic color change which corresponds to a higher visible light absorption as compared to MoS_2-loaded $ZnIn_2S_4$.

Photoluminescence (PL) emission spectra were employed to study the efficiency of photo-generated charge carrier trapping and its recombination rate.[9,24,45] In Fig. 4h, the PL spectrum of $ZnIn_2S_4$ shows a broad peak around 580 nm, which is the main peak attributed to the emission of band gap transition of $ZnIn_2S_4$. Luminescence quenching was observed upon loading of CuS, Ag_2S and MoS_2 co-catalysts. The reduced PL emissions indicate that the charge carrier lifetimes were prolonged and the charge transfers between the photocatalyst and the co-catalyst were promoted. This affirms the function of co-catalysts in suppressing photo-generated charge carrier recombination, thus increasing their photocatalytic activities. Among these three co-catalysts, it can be clearly observed that both CuS and Ag_2S co-catalysts have similar quenching intensities whereas the MoS_2 co-catalyst exhibits a complete quenching. This suggests that the MoS_2 co-catalyst promotes a better charge transfer than CuS and Ag_2S co-catalysts, hence MoS_2 is expected to outperform the other co-catalyst in photocatalysis. Besides that, upon CuS and Ag_2S loading, their PL peak positions were shifted to a higher wavelength, and correspond to the shift in absorption spectra obtained in UV-VIS-NIR spectra.

Fig. 5a shows the photocatalytic H_2 evolution rates during the *in situ* photo-assisted deposition process under visible light irradiation. The maximum H_2 yields from photo-assisted deposition of CuS, Ag_2S and MoS_2 were 3.09, 4.66 and 30.56 μmol h^{-1} respectively, corresponding to a 3-, 5- and 37-fold increase in photocatalytic activities as compared to pristine $ZnIn_2S_4$ microspheres. The stable loading or immobilization of CuS, Ag_2S and MoS_2 co-catalysts and their synergistic effects on photocatalytic properties of $ZnIn_2S_4$ were further confirmed by repeating photocatalytic H_2 evolution after the photo-assisted deposition process (Fig. 5b). In this case, all products obtained after photo-assisted deposition under visible light irradiation were washed before testing for photocatalytic H_2 activity in the presence of UV-visible light irradiation. Similarly, the photocatalytic activities were significantly enhanced in the presence of co-catalysts. This confirms that the enhancement does not originate from the co-catalyst precursors being added into the photocatalytic assay solution but from the photo-deposited co-catalyst. The maximum photocatalytic H_2 evolution yields from UV-visible light irradiation of CuS, Ag_2S and MoS_2 photo-deposited $ZnIn_2S_4$ are 14.95, 15.86 and 47.71 μmol h^{-1} respectively, corresponding to a 7-, 8- and 23-fold improvement over the pristine $ZnIn_2S_4$ microsphere. From Fig. 5a and b, it can be clearly observed

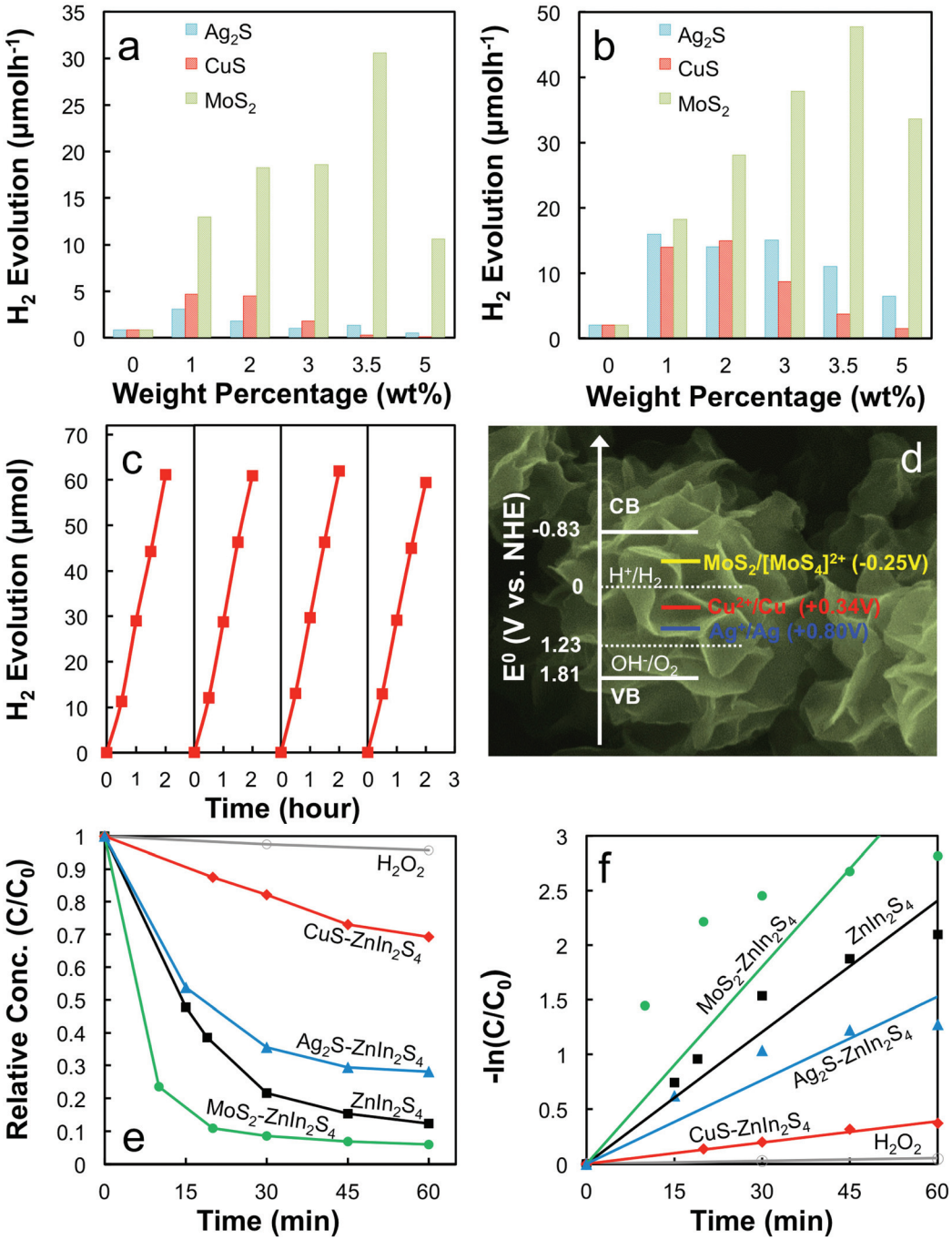

Fig. 5 (a) *In situ* photo-assisted deposition of the co-catalyst and photocatalytic H_2 evolution under visible light irradiation. (b) Photocatalytic H_2 evolution of the photo-deposited $ZnIn_2S_4$ product under UV-visible light irradiation, (c) stability testing over 4 consecutive cycles. (d) Schematic energy band position of the $ZnIn_2S_4$ microsphere and standard reduction potentials of hydrogen, MoS_2, CuS and Ag_2S. (e) Photocatalytic degradation of MO and (f) pseudo-first-order plots of 1 wt% Ag_2S, 2 wt% CuS, 3.5 wt% MoS_2 loaded and unloaded $ZnIn_2S_4$ under visible light irradiation.

that $ZnIn_2S_4$ loaded with MoS_2 consistently shows a better photocatalytic hydrogen production rate than other co-catalysts across all wt% loading. The enhancement of photocatalytic activities in these three co-catalysts can be ranked as MoS_2 being the highest followed by Ag_2S and CuS. The $ZnIn_2S_4$ loaded with MoS_2 exhibits more than 3-fold higher photocatalytic activities than Ag_2S and CuS loaded $ZnIn_2S_4$ and more than 23-fold than pristine $ZnIn_2S_4$. The results ascertain the relatively inexpensive and environmentally-friendly transition metal chalcogenide as an efficient co-catalyst alternative to a Pt or CdS loaded $ZnIn_2S_4$ photocatalysis system.

It is noted that the increase in light absorption generally benefits photocatalytic activities with regard to more photons being absorbed for photocatalytic reaction. However, an exces-

sive increase in co-catalyst loading can adversely affect the photoreactivity due to the following reasons: (i) increase in opacity which leads to a decrease in absorption of the incident light or the so called shading effect[2,45] and (ii) introduction of recombination centers which affect charge mobility.[46,47] Hence, optimized co-catalysts wt% loading for photocatalytic H_2 yield are determined to be 1, 2 and 3.5 wt% for Ag_2S, CuS and MoS_2/$ZnIn_2S_4$ respectively (Fig. 5b). It is noted that the light absorption characteristics of different composite systems do not fully correspond to their photocatalytic activities. Fig. 4e–g show that despite CuS and Ag_2S loading exhibiting higher absorption compared to MoS_2 loading, their photocatalytic activities were not as efficient as MoS_2-loaded $ZnIn_2S_4$. This suggests that other factors may govern the higher photocatalytic activities of MoS_2 over CuS and Ag_2S $ZnIn_2S_4$ composites. The photocatalytic performances correlate with PL results, where a drastic improvement can be seen in MoS_2 loaded $ZnIn_2S_4$ as compared to CuS and Ag_2S loaded $ZnIn_2S_4$. The complete quenching of PL emission of MoS_2 loaded $ZnIn_2S_4$ suggests that the charge carrier lifetime was prolonged and hence significantly improved its photocatalytic performance.

The facet or crystallographic orientation dependence of photocatalytic activities[48–50] has been reported where certain planes show higher photocatalytic activities. According to the work of J. Shen *et al.* on 3D hierarchical $ZnIn_2S_4$, the (006) plane consists of 100% unsaturated coordination In^{3+} and Zn^{2+} cations at the crystal surface.[30,51] These surfaces provide a higher surface energy for effective dissociative adsorption of reactant molecules[50] and separation of photo-excited holes (h^+) and electrons (e^-).[52] The specific plane shows suppressed recombination and enhanced photoreactivity due to affinity towards the sacrificial reagent and acceleration in h^+ consumption.[20] Inevitably, the (006) plane becomes the predominant surface active site for both photo-assisted deposition and photocatalytic H_2 production. While unsaturated cations on the (006) plane consume h^+ and perform oxidation reaction on a sacrificial reagent, the sulfur atoms supply e^- for the reduction of water and metal ions. In a nutshell, the photocatalytic hydrogen production can be attributed to the exposed (006) facet of $ZnIn_2S_4$, as seen in the spectrum of Fig. 4a. From Fig. 4b and c, it can be seen that after CuS and Ag_2S co-catalyst loading, the (006) peak is destructed while the peak is retained after MoS_2 loading. Hence, this may be one of the possible underlying reasons for the $ZnIn_2S_4$ MoS_2 composite outperforming the CuS and Ag_2S loaded $ZnIn_2S_4$ in photocatalytic hydrogen production.

Further, 4 consecutive cycles of photocatalytic H_2 evolution were carried out to explore the stability of photo-deposition of the MoS_2 co-catalyst on $ZnIn_2S_4$ microspheres, with a 2 h cycle (Fig. 5c). It can be observed over 4 cycles that photo-assisted deposition of the co-catalyst on $ZnIn_2S_4$ microspheres shows a consistent photocatalytic H_2 evolution rate with no diminishing photocatalytic activities. This demonstrates the collective stability of $ZnIn_2S_4$ microspheres and the MoS_2 co-catalyst against photocorrosion and detachment from the host microspheres after prolonged photocatalysis. Fig. 5d shows the viability of the transition metal to be reduced by irradiating $ZnIn_2S_4$, where Cu^{2+}, Ag^{2+} and $[MoS_4]^{2+}$ metal ions possess a standard reduction potential lower than the $ZnIn_2S_4$ conduction band.[28,45,46] Under light irradiation, $ZnIn_2S_4$ acquires sufficient chemical potential to perform H_2 evolution as well as electrochemical reduction of metal ions to deposit CuS, Ag_2S and MoS_2 co-catalysts onto $ZnIn_2S_4$ photoactive sites.

Furthermore, photocatalytic MO degradation of all the optimally loaded $ZnIn_2S_4$ composites, *i.e.* 1 wt% Ag_2S, 2 wt% CuS and 3.5 wt% MoS_2, was carried out. As shown in Fig. 5e, MO aqueous solution with added H_2O_2, a strong oxidizer, displays a negligible degradation under visible light irradiation. When $ZnIn_2S_4$ was dispersed into the system, MO concentration dropped to 10% in 1 h. 3.5 wt% MoS_2 loaded $ZnIn_2S_4$ showed the highest photodegradation activity. On the other hand, Ag_2S and CuS loaded $ZnIn_2S_4$ exhibited a slower degradation performance as compared to the pristine $ZnIn_2S_4$, where MO concentrations remained 30 and 70% respectively after 1 h of visible light irradiation. To quantify the kinetics of degradation, the first order rate constants were determined by plotting $-\ln(C/C_0)$ *versus* time, in Fig. 5f where C and C_0 are the MO concentration at a particular instance and the initial MO concentration respectively. The rate constants of pristine $ZnIn_2S_4$, Ag_2S $ZnIn_2S_4$, CuS $ZnIn_2S_4$ and MoS_2 $ZnIn_2S_4$ are 0.0401, 0.0065, 0.0254 and 0.0738, respectively. The best performing MoS_2 $ZnIn_2S_4$ sample displayed an increase of 84% of the degradation rate as compared to pristine $ZnIn_2S_4$. It was reported that the presence of unsaturated surface coordination sites corresponds to an efficient degradation of dye molecules.[36] The result agrees with the XRD data, where only the MoS_2 loaded $ZnIn_2S_4$ preserves the unsaturated surface coordination sites of (006) for improved photodegradation while the Ag_2S and CuS loaded $ZnIn_2S_4$ samples showed diminished diffraction peaks. All the findings unambiguously demonstrate that the *in situ* photo-deposited MoS_2 $ZnIn_2S_4$ microsphere composite shows effective photocatalytic hydrogen production and degradation under visible light irradiation.

4. Conclusions

The combination of simple hydrothermal synthesis of $ZnIn_2S_4$ microspheres together with facile low-temperature *in situ* photo-assisted deposition of CuS, Ag_2S and MoS_2 co-catalysts is demonstrated. The deposited co-catalyst nanoparticles are finely dispersed throughout the host microspheres to optimize contact interfacial charge transfer. The photocatalytic H_2 evolution yield from both UV-visible and visible light irradiation of CuS, Ag_2S and MoS_2 photo-deposited $ZnIn_2S_4$ shows profound improvement (as high as 27-fold) over the pristine $ZnIn_2S_4$ microsphere. The photocatalytic cycling demonstrates the collective stability of $ZnIn_2S_4$ and MoS_2 co-catalysts against photocorrosion and detachment from the host microspheres. Lastly, photocatalytic degradation of MoS_2 loaded $ZnIn_2S_4$ microspheres demonstrated an 84% higher degradation rate than pristine $ZnIn_2S_4$ microspheres.

Acknowledgements

This work was supported by MOE R-263-000-B38-112/R-263-000-B63-112.

References

1 A. Fujishima and K. Honda, *Nature*, 1972, **238**, 37–38.
2 X. Chen, S. Shen, L. Guo and S. S. Mao, *Chem. Rev.*, 2010, **110**, 6503–6570.
3 F. E. Osterloh, *Chem. Mater.*, 2008, **20**, 35–54.
4 A. Kudo and Y. Miseki, *Chem. Soc. Rev.*, 2009, **38**, 253–278.
5 K. Maeda and K. Domen, *J. Phys. Chem. Lett.*, 2010, **1**, 2655–2661.
6 A. Ishikawa, T. Takata, J. N. Kondo, M. Hara, H. Kobayashi and K. Domen, *J. Am. Chem. Soc.*, 2002, **124**, 13547–13553.
7 T. Zhu, C. Zhang and G. W. Ho, *J. Phys. Chem. C*, 2015, **119**, 1667–1675.
8 T. Zhu, K. N. C. Peh, M. Hong and G. W. Ho, *Chem. – Eur. J.*, 2014, **20**, 11505–11510.
9 B. Chai, T. Peng, P. Zeng and X. Zhang, *Dalton Trans.*, 2012, **41**, 1179–1186.
10 Y. Chen, H. Ge, L. Wei, Z. Li, R. Yuan, P. Liu and X. Fu, *Catal. Sci. Technol.*, 2013, **3**, 1712–1717.
11 Z. Lei, W. You, M. Liu, G. Zhou, T. Takata, M. Hara, K. Domen and C. Li, *Chem. Commun.*, 2003, 2142–2143.
12 K. Zhang and L. Guo, *Catal. Sci. Technol.*, 2013, **3**, 1672–1690.
13 S. Shen, L. Zhao and L. Guo, *Int. J. Hydrogen Energy*, 2008, **33**, 4501–4510.
14 X. Gou, F. Cheng, Y. Shi, L. Zhang, S. Peng, J. Chen and P. Shen, *J. Am. Chem. Soc.*, 2006, **128**, 7222–7229.
15 S. Shen, J. Chen, X. Wang, L. Zhao and L. Guo, *J. Power Sources*, 2011, **196**, 10112–10119.
16 S. Shen, L. Zhao, Z. Zhou and L. Guo, *J. Phys. Chem. C*, 2008, **112**, 16148–16155.
17 S. Shen, L. Zhao, X. Guan and L. Guo, *J. Phys. Chem. Solids*, 2012, **73**, 79–83.
18 F. Tian, R. Zhu, Y. He and F. Ouyang, *Int. J. Hydrogen Energy*, 2014, **39**, 6335–6344.
19 X. Zong, H. Yan, G. Wu, G. Ma, F. Wen, L. Wang and C. Li, *J. Am. Chem. Soc.*, 2008, **130**, 7176–7177.
20 L. Wei, Y. Chen, Y. Lin, H. Wu, R. Y and Z. Li, *Appl. Catal., B*, 2014, **144**, 521–527.
21 W. Zhang, Y. Wang, Z. Wang, Z. Zhong and R. Xu, *Chem. Commun.*, 2010, **46**, 7631–7633.
22 J. Meng, Z. Yu, Y. Li and Y. Li, *Catal. Today*, 2014, **225**, 136–141.
23 X. Zong, J. Han, G. Ma, H. Yan, G. Wu and C. Li, *J. Phys. Chem. C*, 2011, **115**, 12202–12208.
24 Y. Chen, G. Tian, Z. Ren, K. Pan, Y. Shi, J. Wang and H. Fu, *ACS Appl. Mater. Interfaces*, 2014, **6**, 13841–13849.
25 J. Zhou, G. Tian, Y. Chen, X. Meng, Y. Shi, X. Cao, K. Pan and H. Fu, *Chem. Commun.*, 2013, **49**, 2237–2239.
26 K. Maeda, K. Teramura, D. Lu, N. Saito, Y. Inoue and K. Domen, *Angew. Chem., Int. Ed.*, 2006, **45**, 7806–7809.
27 L. Ye and Z. Li, *Appl. Catal., B*, 2014, **160–161**, 552–557.
28 H. Tada, M. Fujishima and H. Kobayashi, *Chem. Soc. Rev.*, 2011, **40**, 4232–4243.
29 G. Chen, N. Ding, F. Li, Y. Fan, Y. Luo, D. Li and Q. Meng, *Appl. Catal., B*, 2014, **160–161**, 614–620.
30 J. Shen, J. Zai, Y. Yuan and X. Qian, *Int. J. Hydrogen Energy*, 2012, **37**, 16986–16993.
31 W. L. Ong, S. Natarajan, B. Kloostra and G. W. Ho, *Nanoscale*, 2013, **5**, 5568.
32 J. Zhou, G. Tian, Y. Chen, Y. Shi, C. Tian, K. Pan and H. Yu, *Sci. Rep.*, 2014, **4**, 4027.
33 C. Yu, M. Leng, M. Liu, Y. Yu, D. Liu and C. Wang, *CrystEngComm*, 2012, **14**, 3772–3777.
34 C. Wu, S. H. Yu, S. Chen, G. Liu and B. Liu, *J. Mater. Chem.*, 2006, **16**, 3326–3331.
35 R. Singh and B. Pal, *Part. Sci. Technol.*, 2015, **33**, 53–58.
36 S. Peng, L. Li, Y. Wu, L. Jia, L. Tan, M. Srinivasan, S. Ramakrishna, Q. Yan and S. G. Mhaisalkar, *CrystEngComm*, 2013, **15**, 1922–1930.
37 H. Yu, X. Quan, Y. Zhang, N. Ma, S. Chen and H. Zhao, *Langmuir*, 2008, **24**, 7599–7604.
38 Z. X. Chen, D. Z. Li, W. J. Zhang, C. Chen, W. J. Li, M. Sun, Y. H. He and X. Z. Fu, *Inorg. Chem.*, 2008, **47**, 9766–9772.
39 F. Fang, L. Chen, Y. B. Chen and L. M. Wu, *J. Phys. Chem. C*, 2010, **114**, 2393–2397.
40 K. Cheng and C. Liang, *Sol. Energy Mater. Sol. Cells*, 2010, **94**, 1137–1545.
41 B. Gao, L. Liu, J. Liu and F. Yang, *Appl. Catal., B*, 2014, **147**, 929–939.
42 S. Peng, P. Zhu, S. G. Mhaisalkar and S. Ramakrishna, *J. Phys. Chem. C*, 2012, **116**, 13849–13857.
43 H. Yang, C. Sun, S. Qiao, J. Zou, G. Liu, S. C. Smith, H. Cheng and G. Lu, *Nature*, 2008, **453**, 638–641.
44 Z. Xu, Y. Li, S. Peng, G. Lu and S. Li, *CrystEngComm*, 2011, **13**, 4770–4776.
45 L. Ye, J. Fu, Z. Xu, R. Yuan and Z. Li, *ACS Appl. Mater. Interfaces*, 2014, **6**, 3483–3490.
46 L. Andronic, L. Isac and A. Duta, *J. Photochem. Photobiol., A*, 2011, **221**, 30–37.
47 Q. Wang, G. Yun, Y. Bai, N. An, Y. Chen, R. Wang, Z. Lei and W. Shangguan, *Int. J. Hydrogen Energy*, 2014, **39**, 13421–13428.
48 Y. Bo, S. Ouyang, N. Umezawa, J. Cao and J. Ye, *J. Am. Chem. Soc.*, 2011, **133**, 6490–6492.
49 G. Li, T. Varga, P. Yan, Z. Wang, C. Wang, S. A. Chambers and Y. Du, *Phys. Chem. Chem. Phys.*, 2015, **17**, 15119–15123.
50 X. Gong and A. Selloni, *J. Phys. Chem. B*, 2005, **109**, 19560–19562.
51 W. J. Ong, L. L. Tan, S. O. Chai, S. T. Yong and R. M. Abdul, *Nanoscale*, 2014, **6**, 1946.
52 L. Ye, J. Mao, J. Liu, Z. Jiang, T. Peng and L. Zan, *J. Mater. Chem. A*, 2013, **1**, 10532–10537.

